Electronic Supplementary Material (ESI) for Dalton Transactions.

Supporting Information

for

Highly Porous Palladium Nanodendrites: Wet-chemical Synthesis, Electron Tomography and Catalytic Activity

Stefanos Mourdikoudis,[a,b,c] Verónica Montes-García,[a] Sergio Rodal-Cedeira,[a] Naomi Winckelmans,[d] Ignacio Pérez Juste,[a] Han Wu,[e] Sara Bals,[d] Jorge Pérez Juste,[a]* and Isabel Pastoriza-Santos[a]*

[a] Department of Physical Chemistry and Biomedical Research Center (CINBIO), Universidade de Vigo, 36310 Vigo, Spain.

[b] Biophysics Group, Department of Physics and Astronomy, University College London, London, WC1E 6BT, UK

[c] UCL Healthcare Biomagnetic and Nanomaterials Laboratories, 21 Albemarle Street, London W1S 4BS, UK

[d] EMAT, University of Antwerp, Groenenborgerlaan 171, B-2020 Antwerp, Belgium

[e] Centre for Nature Inspired Engineering (CNIE), Department of Chemical Engineering, University College London, Torrington Place, London, WC1E 7JE, UK

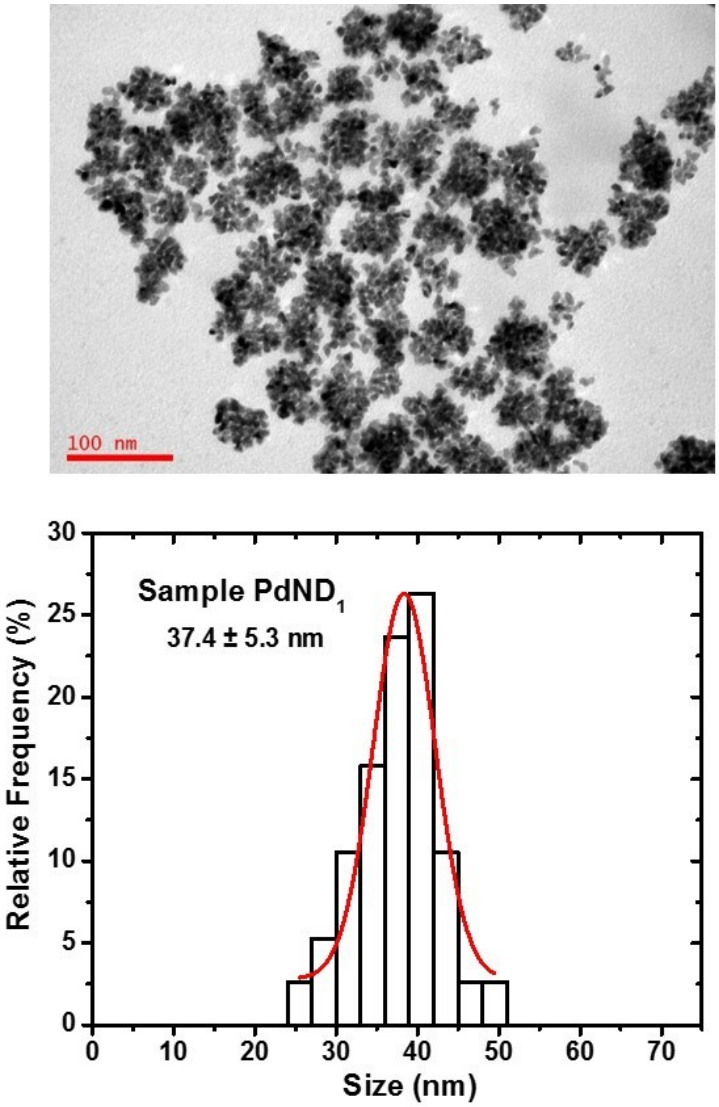

Figure S1. Representative TEM image of $PdND_1$ and the corresponding size distribution histogram.

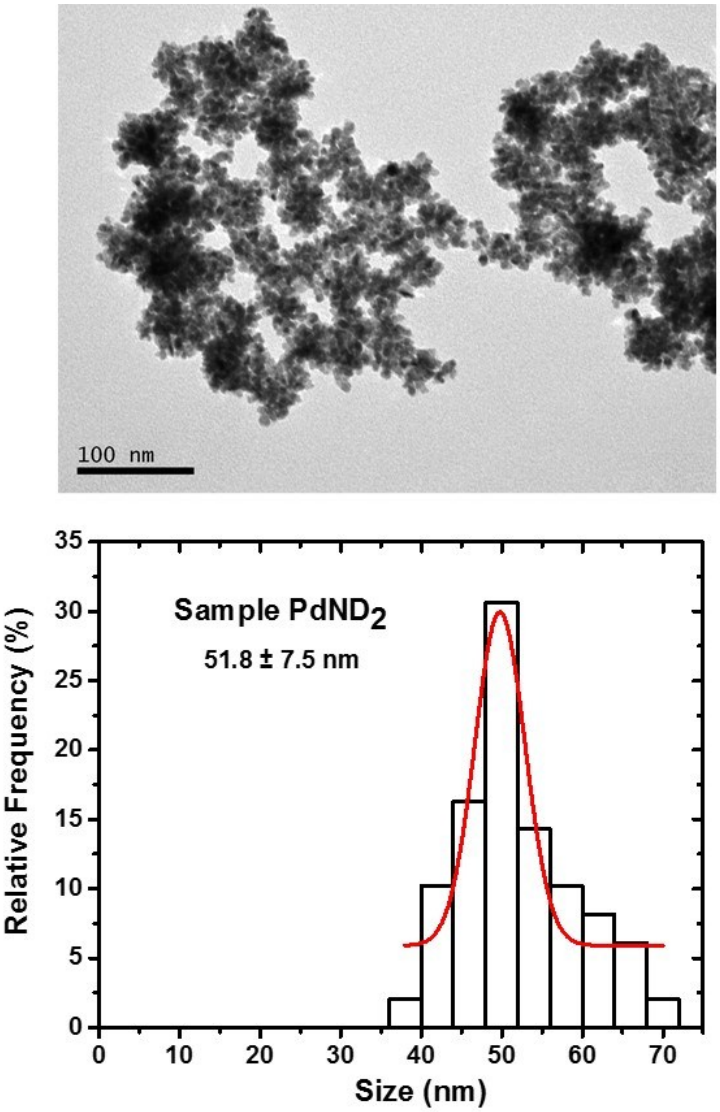

Figure S2. Representative TEM image of $PdND_2$ and the corresponding size distribution histogram.

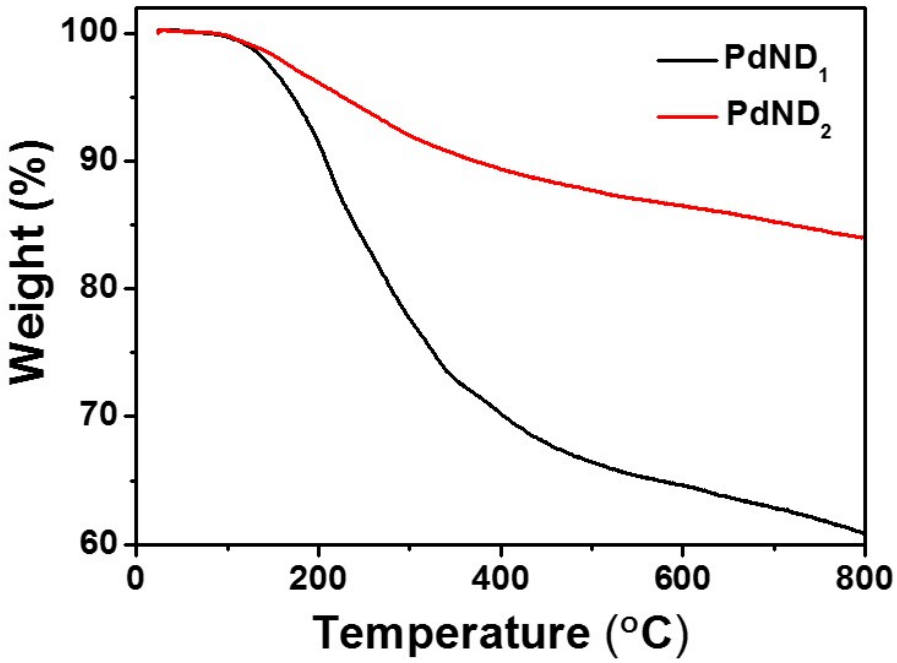

Figure S3. Thermal gravimetric analysis (TGA) of the two types of Pd nanodendrites as indicated.

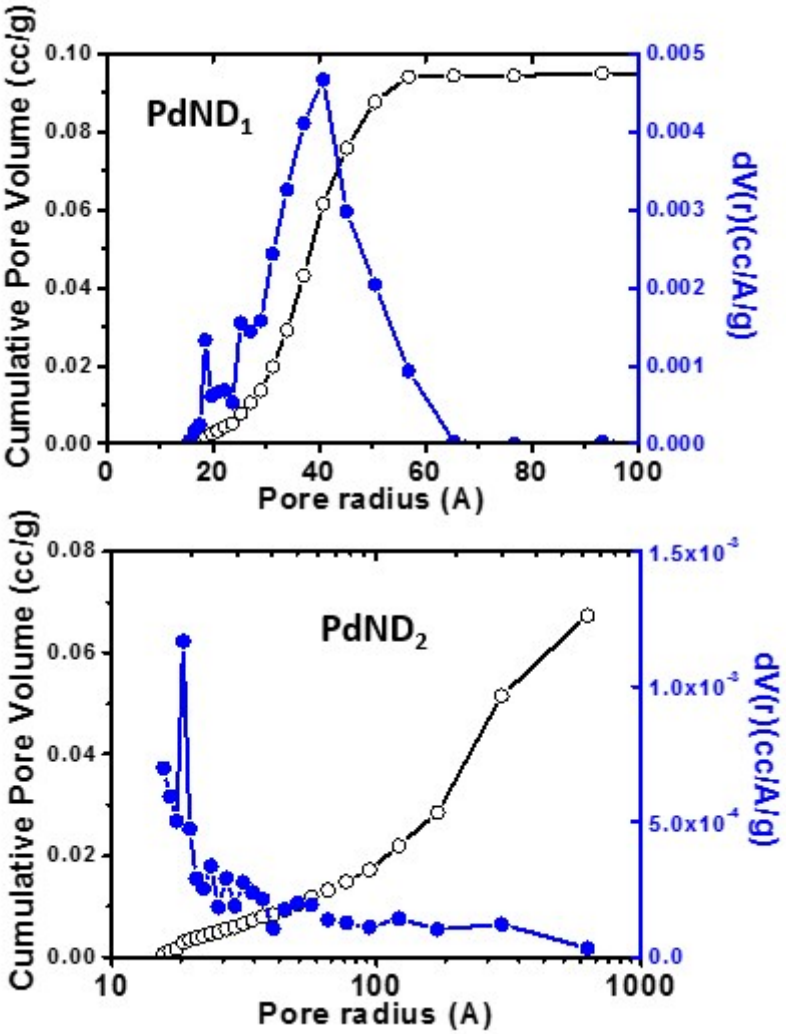

Figure S4. Pore size distribution curves obtained by BET for the samples $PdND_1$ (top) and $PdND_2$ (bottom). The dominant pore size of PdND1 is 8.2 nm whereas the one for PdND2 is 3.7 nm.

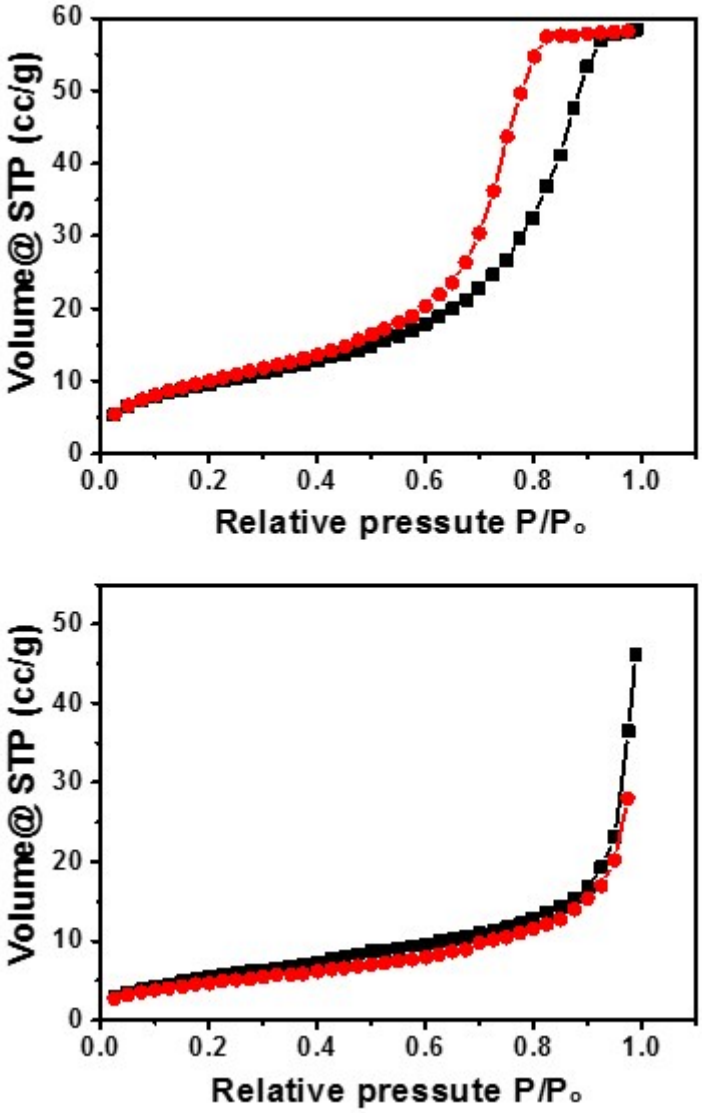

Figure S5. Volume @ STP Vs Relative Pressure (P/Po) for the samples PdND1 (top) and PdND2 (bottom).

The isotherms (Figure S5, top) of sample $PdND_1$ show typical type IV1 mesoporous (2-50) nm sorption behaviour, with capillary condensation at a relative pressure P/Po of between 0.6 and 0.8. The hysteresis loop is characteristic of both type H1 and H2 according to the IUPAC classification.[1] The BJH analysis (Figure S4, top) shows a broad pore size distribution peaking at radius=4 nm (d=8 nm) with no presence of macropores.

The isotherms of $PdND_2$ can be identified as type II isotherms suggesting the physisorption of N_2 of non-porous or macroporous surface. The lack of hysteresis loop and inflection point is due to the absence of mesopores. This can be explained by the BJH analysis revealing very small cumulative pore volume below Radius=5 nm (d =10 nm) and there is no distinct size population above 5 nm region (Figure S4, bottom). The continuous increase of the total pore volume up to R=70 nm is attributed to the

inter-cluster distances rather than the meso/macro pores in the structure. This is in agreement with Electron Tomography analysis at the main manuscript.

$PdND_1$ has much larger surface area (35.3 m^2/g) than $PdND_2$ (17.3 m^2/g) based on multi-point BET analysis. It is clear from both BET and BJH analysis that $PdND_1$ is more porous than $PdND_2$ due to the presence of intra-cluster pore structures at mesoporous range. $PdND_2$ has very small amount of intra-cluster pores at 3.7 nm (indicated by a well-defined peak at about 3.7 nm). However, as there is a known artefact from BJH model fitting at 3.7 nm, due to the breaking of the meniscus of the liquid nitrogen that will always occur at this pressure, the peak is only indicative of the presence of small mesopores or small openings to larger pores.

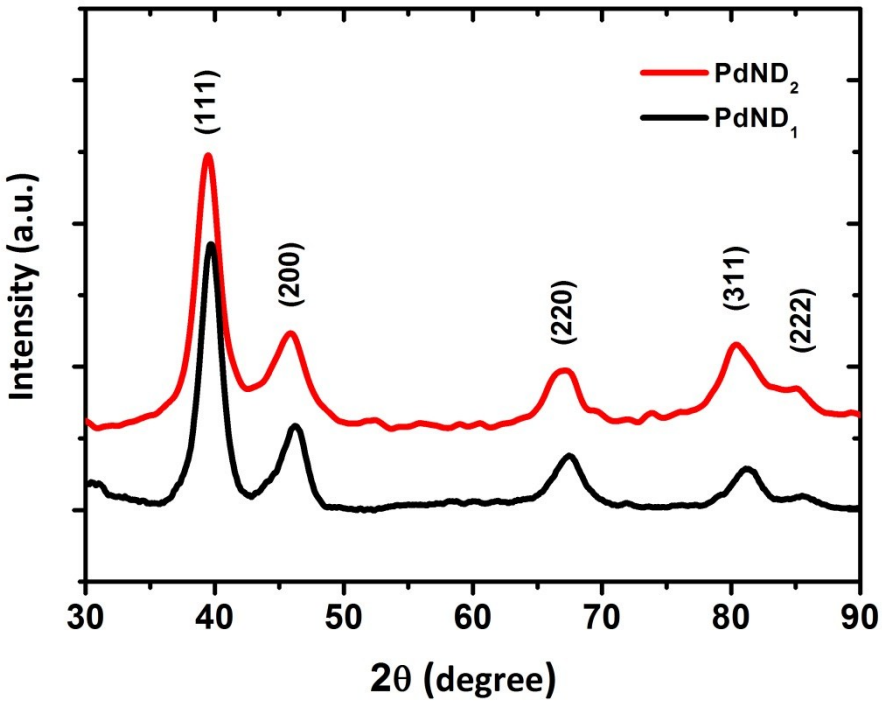

Figure S6. XRD Patterns of $PdND_1$ and $PdND_2$ samples.

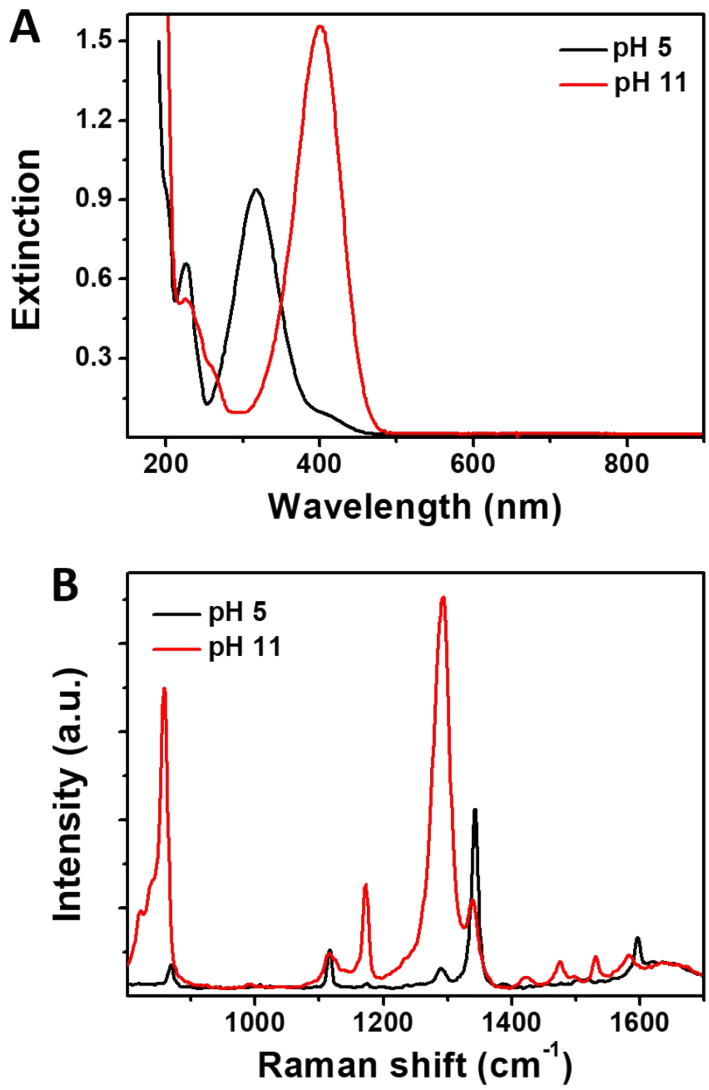

Figure S7. UV-Vis (A) and Raman scattering (B) spectra of 4-NP at pH 5 (black spectra) and pH 11 (red spectra).

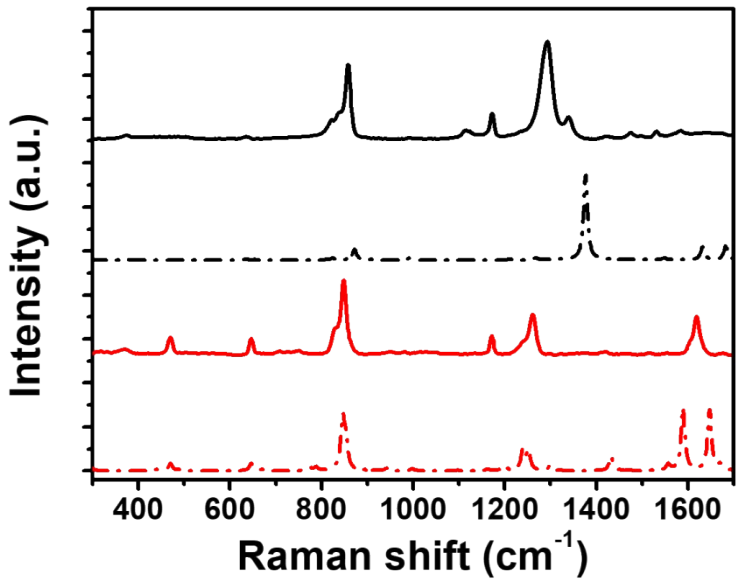

Figure S8. Raman scattering spectra of 4-nitrophenolate ($4\text{-}NP^-$) (black) and 4-aminophenolate ($4\text{-}AP^-$) (red). While solid lines are experimental data, dotted lines are the calculated ones.

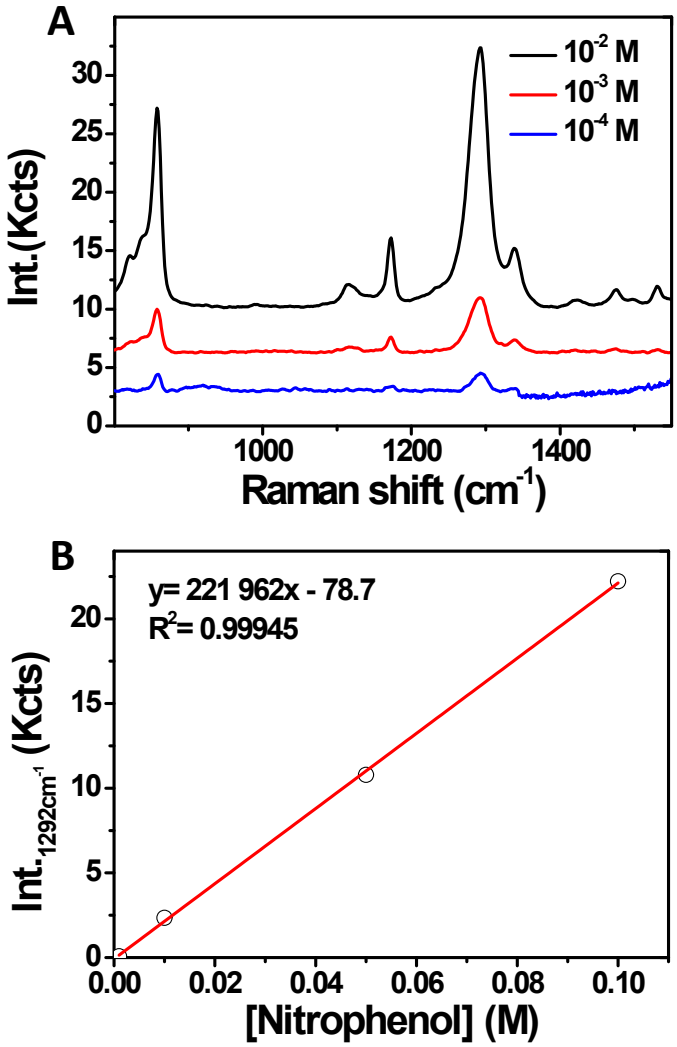

Figure S9. (a) Raman scattering spectra of 4-NP^- at 10^{-2} (black), 10^{-3} (red) and 10^{-4} M (blue). The excitation laser line was 532 nm. (b) Raman intensity (at 1292 cm^{-1}) as a function of 4-NP^- concentration.

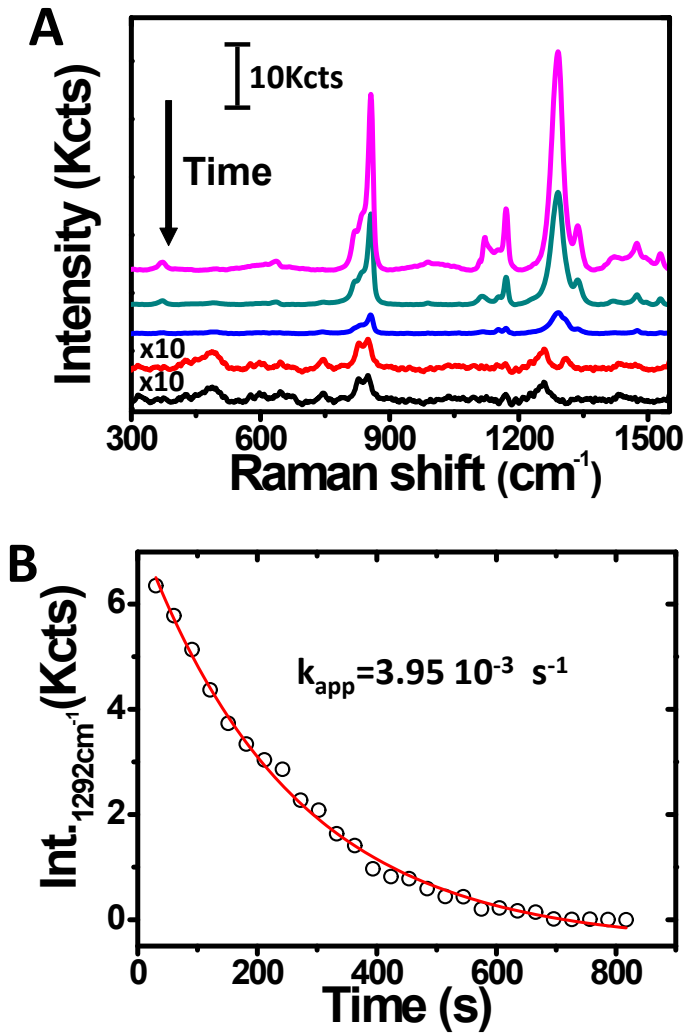

Figure S10. (A) Spectral evolution of a mixture of 4-NP^- and $PdND_1$ upon borohydride addition. [4-NP^-]= 8.2 mM, 0.04 mg of $PdND_1$, [$NaBH_4$]= 77 mM and [NaOH]= 10 mM, T= 25 ºC using Raman scattering spectroscopy. (B) Kinetic trace of the Raman intensity at 1292 cm^{-1} during the reduction of 4-NP^- by $PdND_1$, and linearized data for first-order analysis corresponding to Fig. S6A. The red line represents the best to a first order rate constant.

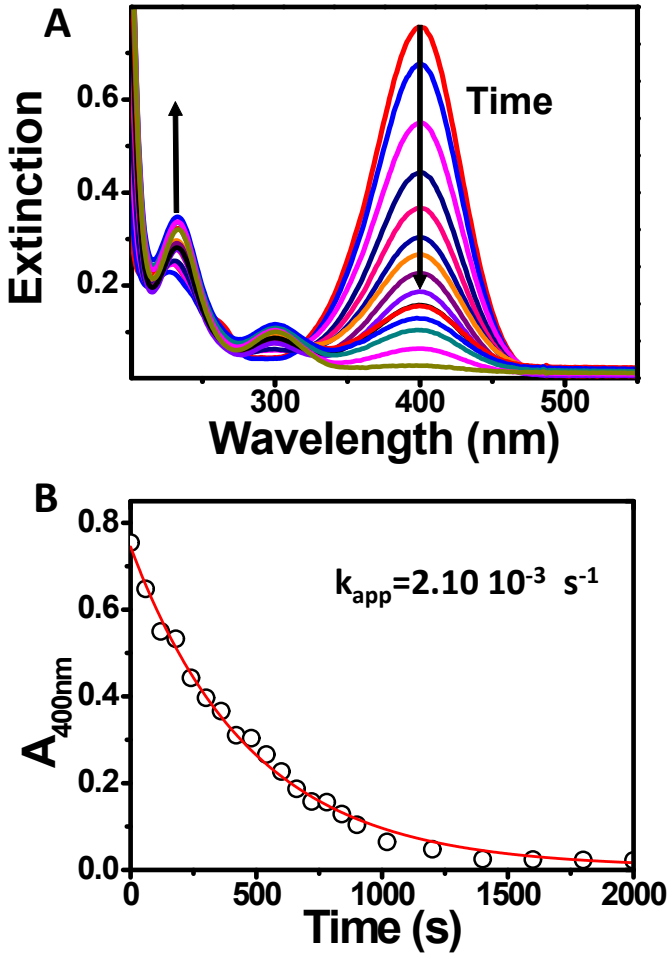

Figure S11. (A) Spectral evolution of a mixture of 4-NP^- and $PdND_1$ upon borohydride addition. [4-NP^-]= 2.76 mM, 0.04 mg of $PdND_1$, [$NaBH_4$]= 77 mM and [NaOH]= 10 mM, T= 25 ºC using UV-Vis spectroscopy. (B) Kinetic trace of the absorbance at 400 nm during the reduction of 4-NP^-. The red line represents the best to a first order rate constant.

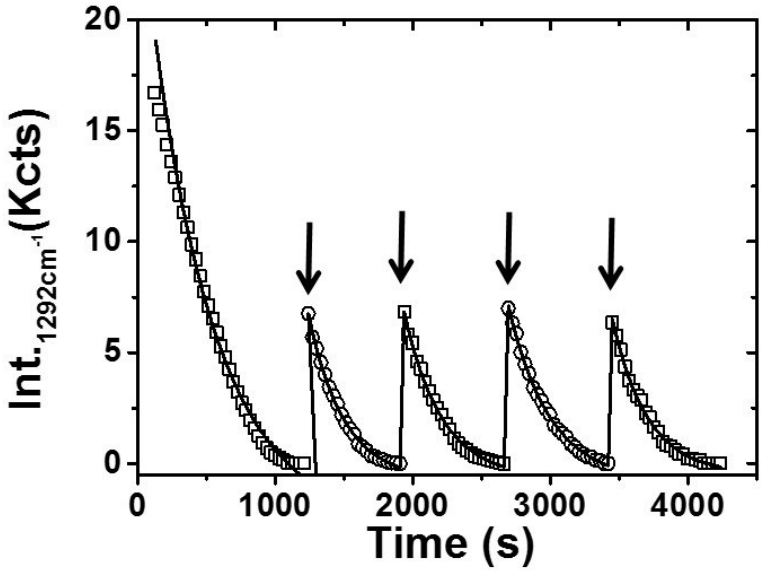

Figure S12. Raman kinetic traces at 1292 cm^{-1}, registered during the sequential reduction of 4-AP^- using $PdND_1$ as catalyst. The arrows indicate the times at which 4-NP^- was added to obtain [4-NP^-]= 2.75 mM and [NaOH]=10 mM. The line represents the best fit to a first-order rate equation.

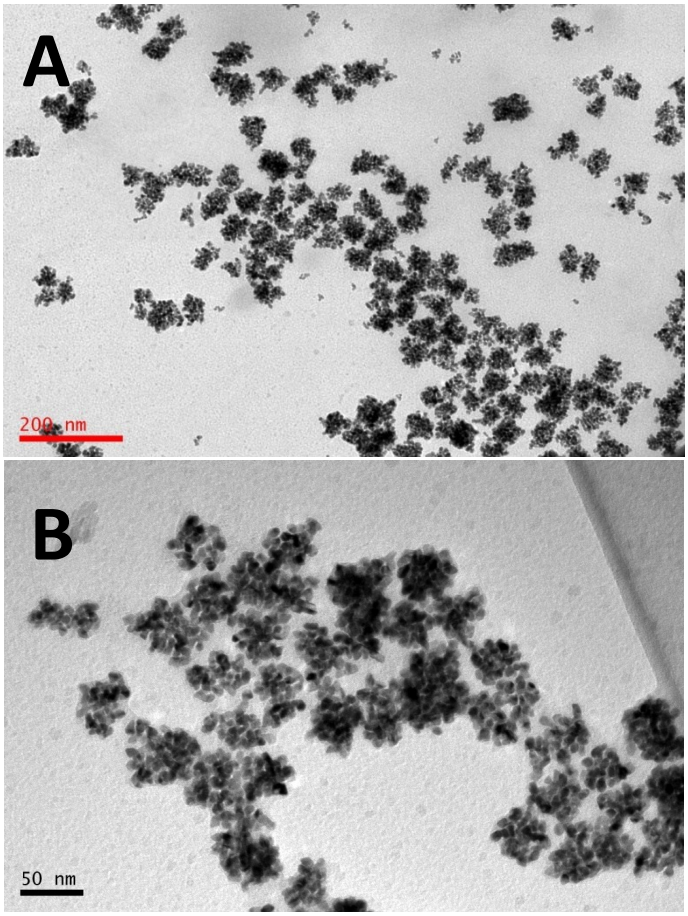

Figure S13. TEM images before (A) and after (B) the use of $PdND_1$ in the catalytic reaction.

Table S1. Summary of the porosities and surfaces areas determined by electron tomography for the different particles analyzed.

	Size (nm)[a]	Sample	Porosity (%)[b]	Active Surface Area (nm^2)[c]
$PdND_1$	37± 5	Tomo1	46 ± 3	10020 ± 140
		Tomo2	53 ± 6	9031 ± 61
		Tomo3	57 ± 8	8768 ± 53
		Tomo4	51 ± 1	7700 ± 42
		Tomo5	40 ± 3	5597 ± 72
$PdND_2$	51 ± 7	Tomo1	33 ± 4	23430 ± 250
		Tomo2	42 ± 3	25030 ± 83
		Tomo3	42 ± 3	70377 ± 53
		Tomo4	38 ± 1	11618 ± 43
		Tomo5	42 ± 1	32017 ± 212

[a] Particle diameter estimated assuming a spherical geometry. [b] Average values measured for each particle, the error takes into account that a missing wedge is present in the experimental series.[2] [b] The highest and lowest values for each type of particle was discarded for estimating the average active surface area.

Table S2. Experimental and calculated vibrational frequencies (cm^{-1}) for 4-NP^-.

Experimental Frequencies (cm^{-1})	**Simulated Frequencies (cm^{-1})**	**Assignation**
373.8	371.05	Ring deformation
	444.98	Ring deformation out-of-plane
	456.13	O=CC bending
634.8	631.3	Ring deformation
	653	Ring deformation
822.2	823.6	Ring deformation
857.9	871.95	ONO bending
	991.75	Ring deformation
1115.6	1112.76	Asymm CCH bending
1172.3	1146.02	Asymm CCH bending
	1209.5	NO stretching + CCH bending
1292.3	1267.15	Asymm CCH bending
1338.6	1334.11	Asymm CCH bending
1422.6	1376.37	NO stretching
1475.3	1436.93	Symm CCH bending
1497.2	1518.94	NO stretching + ring CC stretching
1531	1547.19	Ring CC stretching
1583.3	1605.75	NO stretching + ring CC stretching
1634.2	1631.7	Ring CC stretching + C=O stretching
	1682.13	Ring CC stretching + C=O stretching

Table S3. Experimental and calculated vibrational frequencies (cm^{-1}) for 4-AP^-.

Experimental Frequencies (cm^{-1})	Simulated Frequencies (cm^{-1})	Assignation
317.8	297.01	Ring deformation out-of-plane
369.1	348.19	CCN bending
	438.48	Ring deformation out-of-plane
	469.73	CCO bending+ring deformation
469.2	470.44	Ring deformation
645.8	646.33	Ring twisting deformation
709.0	669.36	Ring deformation out-of-plane
750.3	775.55	Ring deformation
	788.11	Symm HCC bending out-of-plane
	828.11	Ring deformation out-of-plane
847.5	846.16	Ring breathing
847.5	852.96	NH_2 wagging
	941.57	Asymm HCC bending out-of-plane
	997.38	Ring deformation
	1161.51	Symm CCH bending
1171.6	1198.87	NH_2 twisting
1261.0	1239.35	Ring deformation + CCH bending
1261.0	1251.6	Ring deformation + CCH bending
	1299.91	Asymm CCH bending
	1432.16	Symm CCH bending
	1556.4	Asymm ring CC stretch
1618.6	1589.17	C=O strectching + CCH bending (rocking)
	1647.19	NH_2 scissoring bending
	1670.11	Symm ring CC stretching

Table S4. Summary of catalytic performances of different nanomaterials employed for the reduction of 4-NP^- by $NaBH_4$.

Catalyst	k_{nor} (g s^{-1} M^{-1})	Ref.
Pd nanodendrites-1	1274.4	This work
Pd nanodendrites-2	786.5	This work
Pt Nanoflowers	233.3	[3]
Pt black	69.0	[4]
Au@Citrate	27.6	[4]
Ag dendrites	68.9	[5]
Au dendrites	77.5	[5]

References

(1) Thommes, M.; Kaneko, K.; Neimark, A. V.; Olivier, J. P.; Rodriguez-Reinoso, F.; Rouquerol, J.; Sing, K. S. W. Physisorption of Gases, with Special Reference to the Evaluation of Surface Area and Pore Size Distribution (IUPAC Technical Report). *Pure Appl. Chem*. **2015**, *87*, 1051−1069.
(2) Palenstijn, W. J.; Batenburg, K. J.; Sijbers, J. Performance Improvements for Iterative Electron Tomography Reconstruction Using Graphics Processing Units (Gpus). *J. Struct. Biol.* **2011**, *176*, 250-253.
(3) Mourdikoudis, S.; Altantzis, T.; Liz-Marzán, L. M.; Bals, S.; Pastoriza-Santos, I.; Pérez-Juste, J. Hydrophilic Pt Nanoflowers: Synthesis, Crystallographic Analysis and Catalytic Performance *Crystengcomm* **2016**, *18*, 3422-3427.
(4) Lv, J.-J.; Wang, A.-J.; Ma, X.; Xiang, R.-Y.; Chen, J.-R.; Feng, J.-J. One-Pot Synthesis of Porous Pt-Au Nanodendrites Supported on Reduced Graphene Oxide Nanosheets toward Catalytic Reduction of 4-Nitrophenol. *J. Mater. Chem. A* **2015**, *3*, 290-296.
(5) Ye, W.; Chen, Y.; Zhou, F.; Wang, C.; Li, Y. Fluoride-Assisted Galvanic Replacement Synthesis of Ag and Au Dendrites on Aluminum Foil with Enhanced Sers and Catalytic Activities. *J. Mater. Chem.* **2012**, *22*, 18327-18334.